# GEOMETRY IMAGE DIFFUSION: FAST AND DATA-EFFICIENT TEXT-TO-3D WITH IMAGE-BASED SURFACE REPRESENTATION

**Anonymous authors**
Paper under double-blind review

## ABSTRACT

Generating high-quality 3D objects from textual descriptions remains a challenging problem due to high computational costs, the scarcity of 3D data, and the complexity of 3D representations. We introduce **Geometry Image Diffusion** (GIMDiffusion), a novel Text-to-3D model that utilizes geometry images to efficiently represent 3D shapes using 2D images, thereby avoiding the need for complex 3D-aware architectures. By integrating a Collaborative Control mechanism, we exploit the rich 2D priors of existing Text-to-Image models, such as Stable Diffusion, to achieve strong generalization despite limited 3D training data. This allows us to use only high-quality training data while retaining compatibility with guidance techniques such as IPAdapter. GIMDiffusion enables the generation of 3D assets at speeds comparable to current Text-to-Image models, without being restricted to manifold meshes during either training or inference. We simultaneously generate a UV unwrapping for the objects, consisting of semantically meaningful parts as well as internal structures, enhancing both usability and versatility.

## 1 INTRODUCTION

Automatic 3D object generation offers significant benefits across video game production, cinema, manufacturing, and architecture. Despite notable progress in this area, particularly with Text-to-3D diffusion models (Boss et al., 2024; Siddiqui et al., 2024; Wang et al., 2023), generating high-quality 3D objects remains a challenging task due to computational costs, data scarcity, and the complexity of typical 3D representations. For one, it is crucial that the generated objects can be re-lit within graphics pipelines, necessitating the use of physically-based rendering (PBR) materials, for which little data at scale exists. Furthermore, graphics pipelines predominantly use meshes as their primary 3D representation: processing these at scale is notoriously difficult due to their irregular graph structure. Most techniques instead generate an intermediate representation, which increases the burden of training data pre-processing and generated object post-processing.

We propose diffusing joint albedo textures and *geometry images* (Gu et al., 2002), a 2D representation of 3D surfaces, using a Collaborative Control scheme (Vainer et al., 2024). This enables 3D object generation from text prompts, as shown in fig. 1. The image-based representation allows us to repurpose existing image-based architectures, while the Collaborative Control scheme enables us to leverage pre-trained Text-to-Image models, considerably reducing the required training data and costs. Geometry images, and more specifically multi-chart geometry images (Sander et al., 2003), offer two great advantages over other shape representations: they do not impose constraints on the topology of the generated object, and they naturally separate the generated object into semantically meaningful parts, making the objects easier to manipulate and edit. We believe that GIMDiffusion opens up a promising new research direction in Text-to-3D generation, providing a practical and efficient approach that can inspire future advancements in the field. In summary, the advantages of GIMDiffusion include:

- **Image-based**: By leveraging existing 2D image-based models instead of developing new 3D architectures, we simplify both model design and training.
- **Fast Generation**: We generate well-defined 3D meshes in under 10 seconds per object, which could be further enhanced using distillation techniques.

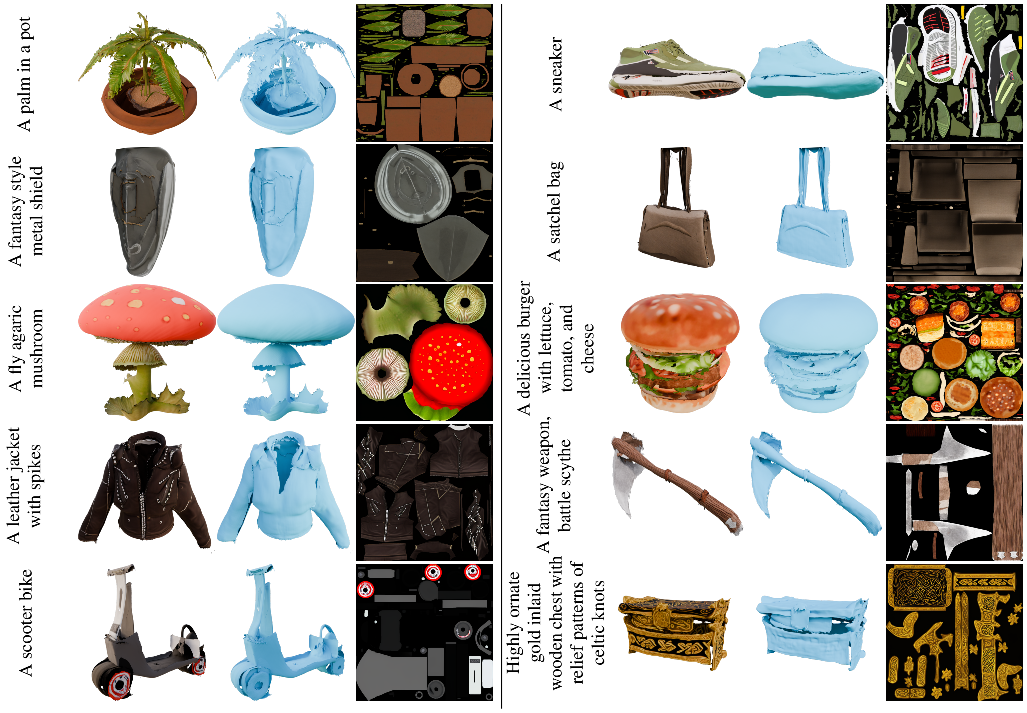
A palm in a pot
A fantasy style metal shield
A fly agaric mushroom
A leather jacket with spikes
A scooter bike
A sneaker
A satchel bag
A delicious burger with lettuce, tomato, and cheese
A fantasy weapon, battle scythe
Highly ornate gold inlaid wooden chest with relief patterns of celtic knots

Figure 1: The objects are generated entirely using our method, including the structure, texture, and UV map layout, all created completely from scratch. For each object, we show the generated albedo texture, the textured mesh, the untextured mesh, and the respective text prompt.

- **Generalization**: Through collaborative control, we reuse pre-trained Text-to-Image priors, allowing for strong generalization beyond our limited 3D training data.
- **Separable Parts**: GIMDiffusion creates assets that consist of distinct, semantically-meaningful, separable parts, facilitating easier manipulation and editing.
- **Albedo Textures**: The 3D assets generated by GIMDiffusion do not have baked-in lighting effects, making them directly suitable for graphics pipelines.
- **UV unwrapping**: Our method jointly generates a UV unwrapping for the objects, learned from the training dataset. To the best of our knowledge, this is the first Text-to-3D method capable of achieving this.
- **Direct geometry**: Our 3D assets do not require the application of iso-surface extraction algorithms, which reduces potential artifacts and simplifies the overall workflow.

## 2 Related Work

### 2.1 Text-to-Image Generation

Diffusion models (Sohl-Dickstein et al., 2015; Song et al., 2020) and flow matching (Lipman et al., 2022), alongside the rise of versatile, general-purpose architectures such as transformers (Vaswani et al., 2017), have brought considerable progress in generative modeling. In particular, text-conditioned image generation was revolutionized by approaches based on Latent Diffusion (Rombach et al., 2021) and its further extensions (Podell et al., 2023; Pernias et al., 2024; Esser et al., 2024). Foundational models like Stable Diffusion, trained on extensive internet-scale datasets (such as LAION-5B (Schuhmann et al., 2022)), are capable of generating complex scenes from text prompts while exhibiting an implicit understanding of scene geometry. Due to the high cost of training such models, they are often repurposed for other tasks or modalities (Zhang et al., 2023; Hu et al., 2023; Ke et al., 2023). Our proposed GIMDiffusion is a prime example of this, as it adapts the base model to specifically output albedo textures.

### 2.2 Conditioning Diffusion Models

Control mechanisms modify pre-trained foundational models, enabling them to accept additional conditions. Existing pixel-aligned control techniques fall into two categories: fine-tuning the base model with modified input and output spaces (Duan et al., 2023; Ke et al., 2023), or a separate model that alters the base model's internal states (Zhang et al., 2023; Zavadski et al., 2023). The latter approaches, such as ControlNet (Zhang et al., 2023), have gained wide adoption due to their ability to preserve the original model's performance while adding conditions such as human poses or depth images. AnimateAnyone (Hu et al., 2023) leverages a similar architecture to inject the base model's hidden states into a new branch that aligns with the base model's output.

In our method, we need to both control the base model (which will output UV-space albedo textures) and extract significant features from it (to generate the geometry image modality). Collaborative Control (Vainer et al., 2024) achieves exactly this by introducing bidirectional communication between both models, originally designed for Text-to-PBR-Texture generation.

### 2.3 Text-to-3D generation

We identify two main approaches to Text-to-3D generation: optimization-based and feed-forward methods. *Optimization-based* methods adapt 2D diffusion models to 3D by applying score distillation sampling (SDS) (Poole et al., 2022; Wang et al., 2022; 2023) to iteratively optimize a 3D scene, represented e.g. by NeRF (Mildenhall et al., 2020) or Gaussian Splats (Kerbl et al., 2023). These methods can produce content of high perceptual quality, but at the cost of impractically long generation times (Lorraine et al., 2023; Xie et al., 2024). The key advantage of this approach is its ability to utilize the rich 2D prior, allowing for 3D object generation without the need for expensive 3D data.

However, the lack of camera conditioning leads to discrepancies among different viewing angles (Janus effect (Poole et al., 2022)) and projection artifacts. To mitigate these issues, 3D-aware architectures and retraining on restrictive 3D datasets are often used, which can weaken the 2D prior (Shi et al., 2023b; Liu et al., 2023; Höllein et al., 2024; Zheng & Vedaldi, 2023; Shi et al., 2023a; Kant et al., 2024). Additionally, the original SDS formulation can lead to issues such as saturated colors, oversmooth geometry, and limited diversity (Wang et al., 2023; Zhu et al., 2023; Katzir et al., 2023; Alldieck et al., 2024; Liang et al., 2023; Wu et al., 2024).

*Feed-forward* methods directly generate 3D shapes without the need for iterative refinement. These methods employ complex, specialized architectures and typically require training on expensive 3D data from scratch. While seminal works like Point-E (Nichol et al., 2022) and its follow-ups (Huang et al., 2024; Zeng et al., 2022) demonstrate impressive generalization and diversity, the inherent lack of connectivity information limits the expressiveness of point clouds. Instead, many current methods rely on other proxy representations, such as neural implicits (Xie et al., 2021; Mildenhall et al., 2020; Malladi et al., 1995; Jun & Nichol, 2023; Zheng et al., 2022; Chen & Zhang, 2018; Mescheder et al., 2018; Yariv et al., 2023) or triplanes (Hong et al., 2023; Chan et al., 2021; Tochilkin et al., 2024; Boss et al., 2024; Bensadoun et al., 2024), to represent the objects.

Both groups of methods require pre- and post-processing to transform between the mesh domain and the proxy representation, e.g. through marching cubes (Lorensen & Cline, 1987) or tetrahedra (Doi & Koide, 1991). This process is costly and lossy, introducing issues such as quantization or grid-like artifacts, and leading to information loss, the loss of part segmentation and internal structures. Moreover, generated objects often require UV unwrapping, a complex post-processing step, for use in artist workflows. In contrast, our model jointly generates the UV map along with the object shape, requiring only a simple triangulation step.

### 2.4 Geometry Images

Geometry images (GIMs) (Gu et al., 2002; Sander et al., 2003) have been largely overlooked in deep learning (Sinha et al., 2016). XDGAN (Alhaija et al., 2022) is a pioneering effort that utilizes GIMs as the representation of choice for a StyleGAN-based architecture (Karras et al., 2018). However, due to the architectural constraints, the training data must be perfectly aligned with a template atlas, which limits its applicability to real-world data. Furthermore, the pre-processing algorithm provided in the paper is restricted to shapes of genus zero — Section 3.3.2 shows how to handle arbitrary shapes.

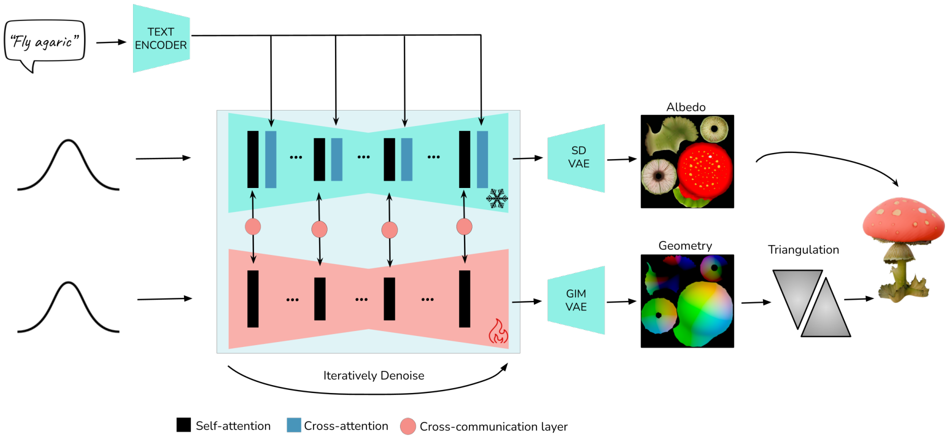

Figure 2: The method overview. Two separate diffusion models generate respectively albedo textures and geometry images. The former is a frozen pre-trained model, while the latter is an architectural clone trained from scratch. Models interact via the Collaborative Control Scheme. To obtain a mesh, generated geometry image is triangulated with the algorithm described in section 3.3.3

Recent concurrent work (Yan et al., 2024) has advocated for low-resolution $64 \times 64$ geometry images as a 3D representation for class-conditioned diffusion models and highlights its efficiency on a small-scale dataset of $8000$ objects (Collins et al., 2021), albeit with limited generalization. In contrast, GIMDiffusion addresses general Text-to-3D: rather than training a model from scratch, we leverage a pre-trained Text-to-Image diffusion model (using a Collaborative Control scheme trained on Objaverse (Deitke et al., 2022)) to retain generalization and diversity in the shapes, their appearance, *and* the UV atlas layout.

# 3 METHOD

## 3.1 GEOMETRY IMAGES

Geometry images (Gu et al., 2002) encode 3D surfaces in image format. This is achieved by a mapping function $\phi : [0,1]^2 \to S \subset \mathbb{R}^3$, where $S$ denotes the 3D surface, and $[0,1]^2$ represents the UV coordinates in the unit square, typically sampled on a uniform grid of the desired resolution. The function $\phi$, also known as a *surface parametrization* (Floater & Hormann, 2005), The choice of $\phi$ is crucial and is usually designed to minimize spatial distortion (e.g. conformal mapping).

Unlike 3D meshes, which require explicit data structures to maintain connectivity, geometry images implicitly connect each pixel to its neighbors. Gu et al. (2002) tackled surface mapping by cutting the input surface and warping it onto a disc, but this approach is limited to manifold objects and introduces significant distortions for high-genus shapes. Multi-Chart Geometry Images (Sander et al., 2003) address this limitation by mapping surfaces piecewise onto multiple charts of arbitrary shape, each homeomorphic to a disc. This approach adds flexibility (removing the manifold constraint) and reduces distortion (providing greater geometric fidelity). However, Multi-Chart Geometry Images lack connectivity information between charts and are susceptible to sampling artifacts, which can lead to visible cracks along boundaries, as discussed in section 4.5. Additionally, the algorithm proposed to construct $\phi$ is restricted to well-behaved manifold meshes. The optimal surface parametrization remains an active area of research (Sawhney & Crane, 2017; Srinivasan et al., 2023).

Most available 3D meshes have textures applied through UV maps. We observe that these handcrafted maps can be used to construct a desirable multi-chart $\phi$. Beyond providing low-distortion mappings, these UV maps strategically place chart boundaries in locations optimal for animation and downstream processing tasks. Furthermore, charts in handcrafted UV maps often *carry semantic meanings*, which propagate to the output of our model. This is evident in fig. 3, where the hands, face, and various parts of the gunslinger's appearance are separated in the UV atlas.

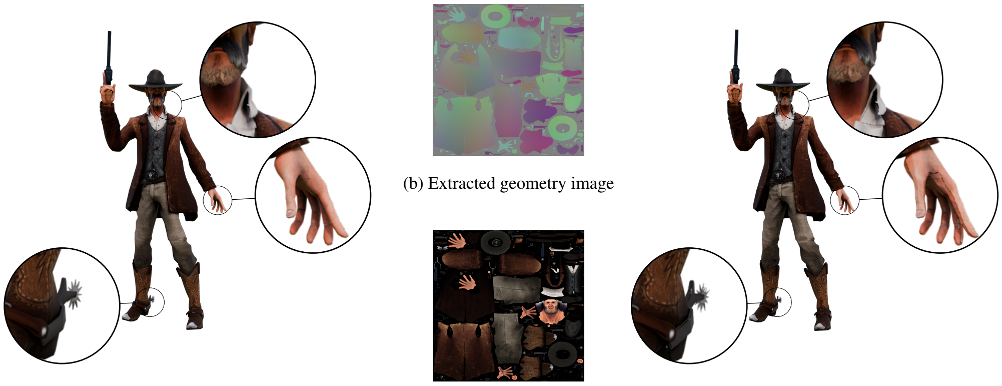

(b) Extracted geometry image

(a) Input mesh

(c) Extracted albedo texture

(d) Reconstructed mesh

Figure 3: (a) Ground-truth geometry, (b) geometry image and (c) albedo texture from our data preprocessing, and (d) the reconstruction using our dedicated VAE. We note the highly separable nature of the ground truth object, which is split into small components. The only visible artifact after decoding is the missing connection between charts of the geometry image, as discussed in sections 3.3 and 4.5.

As the density of the generated geometry's triangulation is limited by the resolution of the underlying geometry image, we follow Rombach et al. (2021) and use a VAE to increase the effective resolution of our model. To address the irregularities in geometry images and better match their distribution — particularly the need to accurately reconstruct the discontinuities at the boundaries of the charts — we add a channel to represent the multi-chart mask and modify the loss function accordingly. Otherwise, we follow the VAE training procedure from StableDiffusion1.5 (Rombach et al., 2021), leaving out only the GAN and LPIPS losses (see details in appendix A). As shown in fig. 3, the reconstruction using this VAE reconstructs everything well, except for the missing connections between the charts.

### 3.2 Collaborative control

To leverage the prior knowledge encoded in existing 2D Text-to-Image models, we use the Collaborative Control approach (Vainer et al., 2024). As shown in fig. 2, this approach comprises two parallel networks: a pre-trained RGB model and a new model for the geometry image. The former is responsible for generating UV-space albedo textures, while the latter generates the geometry images. These two models are connected by a simple linear cross-network communication layer, which allows them to share information and collaborate in generating pixel-aligned outputs across these different modalities. Crucially, this also enables the geometry model to influence the frozen model, guiding it to generate UV-space textures that would otherwise lie at the fringes of its training distribution. The frozen base model also drastically reduces the amount of data required to train the joint model while retaining generalizability, diversity, and quality (Vainer et al., 2024).

### 3.3 Data Handling

#### 3.3.1 Dataset

We train our model on the Objaverse dataset (Deitke et al., 2022). We curate this dataset to include only objects with both high-quality structures and semantically meaningful UV maps by filtering out 3D scans and low-poly models. The final dataset contains approximately 100,000 objects. Each data entry is accompanied by captions provided by Cap3D (Luo et al., 2023) and Hong et al. (2024). During training, we randomly sample these captions and apply random rotations of 90, 180, or 270 degrees to the extracted texture atlases. We now discuss how to transform these meshes into geometry images and back: the entire pre-processing was performed on consumer-grade PC hardware (AMD Ryzen 9 7950X, GeForce RTX 3090, 64 GB RAM) and took approximately 20 hours.

#### 3.3.2 Geometry Image Creation

To create Multi-Chart Geometry Images for 3D meshes, we use their existing UV maps. UV mapping is defined as the mapping $\rho : V \rightarrow [0, 1]^2$, where $V$ is the set of vertices in a 3D mesh, and $\rho$ maps each vertex to UV coordinates. Note that this mapping is not injective (multiple vertices can be mapped to the same UV coordinates), nor is it a simple function of the vertex positions in $\mathbb{R}^3$, as modern mesh formats allow multiple vertices with distinct UV coordinates at the same 3D location. These issues mean that $\rho$ is not invertible, which would be a simple way to create a geometry image function. However, we argue that $\rho$ is *locally invertible* and propose constructing a Multi-Chart Geometry Image based on the individually invertible areas of the available UV mapping. As mentioned before, the charts in a UV atlas tend to be semantically meaningful, so we aim to preserve them.

We begin by identifying the connected components of the mesh, which provides an initial separation into charts. Within each component, we identify two situations where $\rho$ is not invertible: duplicated vertices with distinct UV coordinates, and a "crease", i.e. a line where the UV coordinates change direction (similar to a "mirror" boundary condition). The former is straightforward to detect, as we can find duplicated vertex positions with different UV coordinates. The second case is identified by creating a heatmap of the UV space access pattern and detecting local minima, which indicate an indexing pattern that "doubles back" on itself. We then further split the individual charts along any detected creases. In line with the desirable mapping properties discussed in (Sinha et al., 2016), we adjust the geometry image mapping to approximate an equal-area projection by rescaling each 2D chart with respect to the area of the corresponding surface.

In cases where only a partial UV mapping is available, we use XAtlas (Young, 2022) to UV-unwrap the missing regions. However, since the XAtlas parametrization is of lower quality and lacks semantic properties, we exclude meshes where less than $80\%$ of the surface area has been unwrapped manually. This simple heuristic allows us to construct multi-chart geometry images for nearly all training examples. However, this method does not account for all possible degenerate cases of $\rho$. Therefore, we verify that the constructed $\rho$ is injective and skip any training meshes where this assumption is violated.

In Objaverse (Deitke et al., 2022), the objects are not aligned in a canonical way. Although most shapes are oriented with the Y-axis pointing upward, there is no fixed front view, leading to rotational ambiguity between the X- and Z-axes. To resolve this ambiguity and confine it to a single coordinate, we leverage cylindrical coordinates $(r, \theta, \phi)$ so that the ambiguity is restricted to the azimuth angle $\theta$.

### 3.3.3 Mesh Extraction

As mentioned in section 3.1, geometry images implicitly encode connectivity information of the mesh by treating neighboring pixels as connected in 3D space, i.e. a quad mesh. However, to convert them into a more widely supported triangular mesh, we need to specify exactly how to triangulate the quads. For this, we closely follow the algorithm from Sander et al. (2003). For any $2 \times 2$ block of pixels in the GIM, we create up to two triangles depending on how many of the pixels describe part of the object. If necessary, the quad is split along its shorter diagonal. As shown in fig. 4, and in line with our goal of area-preserving mapping (Sinha et al., 2016), the resulting triangulation is nearly uniform over the surface, which may or may not be desirable for specific applications. With our model's working resolution of $768 \times 768$, our GIMs can encode meshes with up to 589,824 vertices. We consider the generation of arbitrary topologies or mesh generation with polygon constraints a promising area of future work for GIMDiffusion.

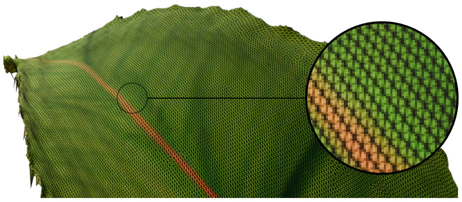

Figure 4: The resulting triangulation of our generated objects is nearly uniform across the surface, due to the area-preserving nature of the geometry images in our training dataset.

### 3.4 Training

For the frozen base model, we used a zero-terminal-SNR (Lin et al., 2024) version fine-tuned from StableDiffusion v2.1 (Rombach et al., 2021) as the base Text-to-Image model, which remains frozen and generates albedo textures. The geometry model is an architectural clone with the cross-attention layers omitted and is trained from scratch, along with the cross-network communication layers. Initially, we trained the model at $256 \times 256$ resolution for $250{,}000$ steps with a batch size of $384$, and then at the final output resolution of $768 \times 768$ for a total of $100{,}000$ steps with a batch size of $64$. All stages of training were conducted with a learning rate of $3e^{-5}$ on 8 A100 GPUs.

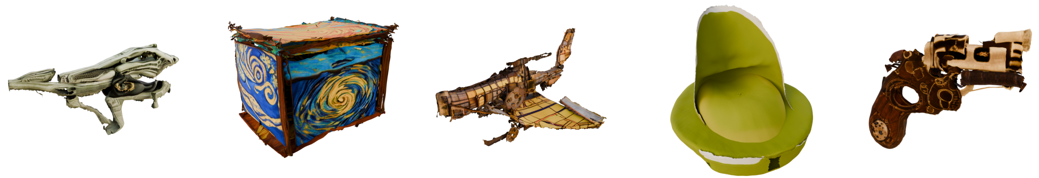

*An organic alien gun is style of H.R. Giger*

*Wooden chest with Van Gogh's Starry Night*

*A steampunk airplane*

*An avocado-shaped chair*

*A steampunk gun*

Figure 5: GIMDiffusion generalizes well beyond the training data, successfully following more outlandish prompts.

## 4 Results

Figure 1 showcases the results of our method on a set of text prompts, generating objects in a manner that aligns with common queries, such as those in a gaming workflow. The objects are **well-defined** and can be **relit from any direction**, as the albedo textures are free from lighting-related artifacts. The generated UV layouts closely resemble those created by artists, offering editable assets.

In fig. 6 we highlight the method's ability to generate meaningful variations when the seed or prompt is perturbed. GIMDiffusion produces significantly different UV layouts with even slight variations in the seed or prompt, enabling diverse object creation. Leveraging the rich natural image prior, our model generalizes well beyond the initial 3D dataset (see appendix E for the layout novelty study). Further examples illustrating this generalization are shown in fig. 5.

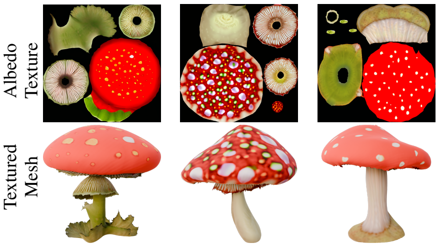

**Prompt:** *A fly agaric mushroom*

Figure 6: Sample diversity of GIMDiffusion for different random seeds.

### 4.1 Separability and Internal Structure

A key advantage of our method is its ability to generate objects divided into distinct semantic (or nearly semantic) parts, as shown in fig. 7, making the generated objects more suitable for editing and animation. This capability arises from the multi-chart representation design and the semantic information embedded in the training data through handcrafted UV maps, which loosely correspond to the semantic components of objects. This approach also allows users to easily correct imperfections, such as misaligned parts or extraneous geometry, and even combine different parts from multiple generations. Additionally, our method generates internal structures, such as the filament inside a light bulb or the interior of a fish tank, because geometry images represent the entire object holistically, not just its visible surfaces.

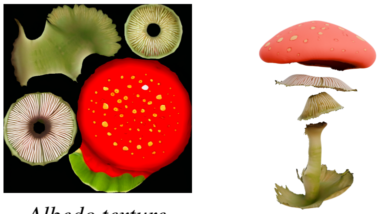

*Albedo texture*

*Exploded view*

Figure 7: An exploded view of the generated "Fly agaric mushroom" shows semantically meaningful chart separation.

### 4.2 IPAdapter Compatibility

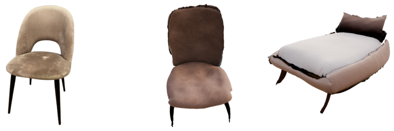

IPAdapter input

*<No prompt>*

*A kingsize bed*

Figure 8: We can guide the reverse process by applying a pre-trained IPAdapter to the frozen base model (Ye et al., 2023).

Major efforts have been made to achieve style control in diffusion models (Ye et al., 2023), and our method is compatible with these techniques. Since we leverage a frozen base model to generate the albedo textures, we can apply a pre-trained IPAdapter and produce stylized output meshes, as shown in fig. 8. Despite the significant mismatch between the application domains (natural images versus albedo atlases), the style guidance remains successful. However, we find that this approach starts to break when the text prompt deviates too much structurally from the content of the conditioning image. We attribute this to the fact that IPAdapter aims to leverage every aspect of the conditioning image; but e.g. IPAdapterInstruct (Rowles et al., 2024) offers a selective extraction of just appearance style without entangling structural information.

### 4.3 Evaluation

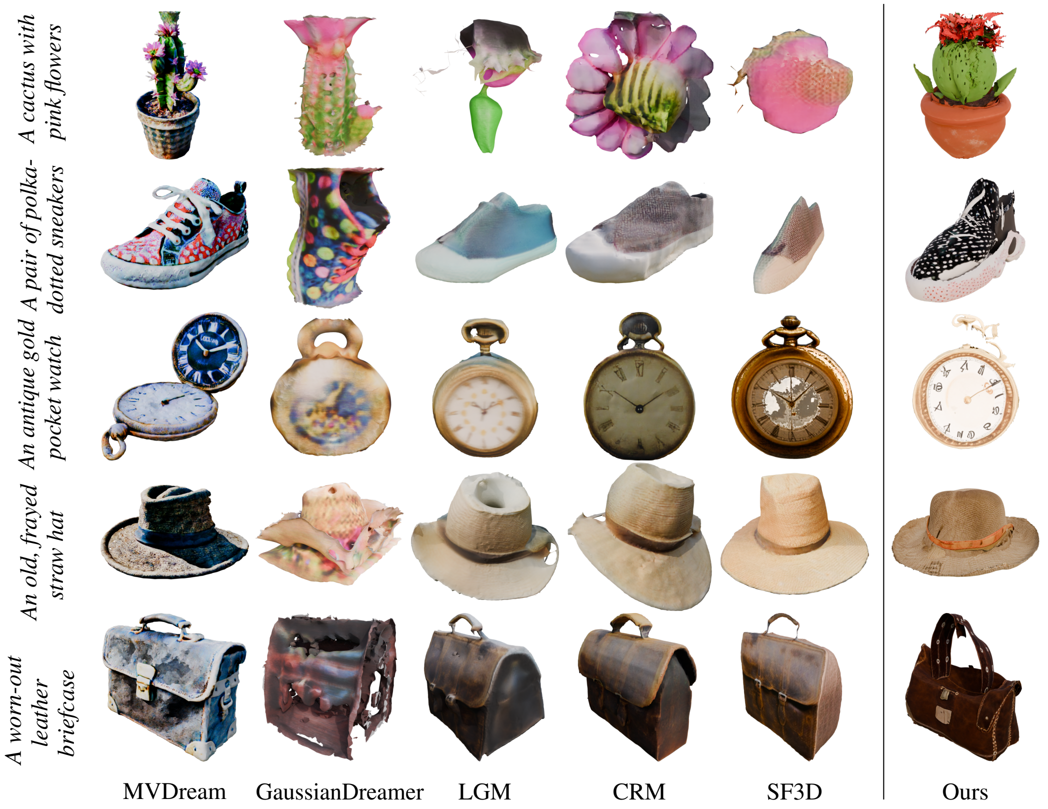
A cactus with pink flowers
A pair of polka-dotted sneakers
An antique gold pocket watch
An old, frayed straw hat
A worn-out leather briefcase
MVDream
GaussianDreamer
LGM
CRM
SF3D
Ours

Figure 9: The qualitative evaluation on prompts from T$^3$Bench (He et al., 2023). Note that our model produces well-defined shapes and detailed appearances due to high-resolution of underlying geometry images. The only noticeable defects are visible cracks and minor misplacements of small parts, which we aim to address in future work (see section 4.5).

We selected several recent works with available source code for comparison, including both optimization-based and feed-forward methods. Specifically, we chose GaussianDreamer (Yi et al., 2023), DreamGaussian (Tang et al., 2023), MVDream (Shi et al., 2023b), LGM (Tang et al., 2024), CRM (Wang et al., 2024) and SF3D (Boss et al., 2024). We adapted state-of-the-art Image-to-3D models LGM, CRM and SF3D for Text-to-3D by integrating the same Text-to-Image model used in our approach (see more details on evaluation in appendix C).

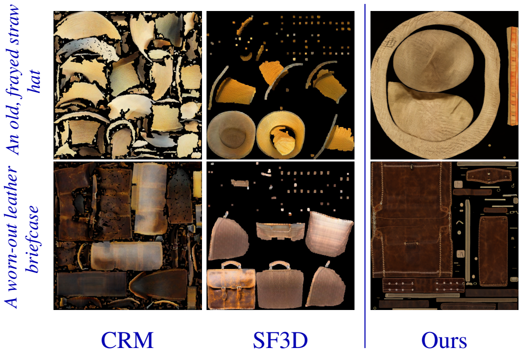

Figure 10: Our method generates layouts of higher quality than parametrization algorithms used in other methods.

We treated the 3D mesh as the final output[1] and included post-processing time in the total generation time, using default settings for all methods. For Image-to-3D models, we also accounted for

[1] GaussianDreamer outputs Gaussian splats, which we converted using the method provided by LGM for evaluation

Table 1: Evaluations

| Method | Time | UV-unwrapping | Relightable | Separable | $T^3$ ↑ | AR > 4 (%) ↓ | RR > 4 (%) ↓ | MA < 10 (%) ↓ |
|---|---|---|---|---|---|---|---|---|
| GaussianDreamer | 15 minutes | No | No | No | 28.7 | - | - | - |
| MVDream | 30 minutes | XAtlas | No | No | 47.8 | - | - | - |
| DreamGaussian | 7 minutes | XAtlas | No | No | 19.8 | - | - | - |
| LGM | 1.8 minutes | XAtlas | No | No | 29.9 | 0.068 | 0.081 | 0.060 |
| CRM | 13 sec | XAtlas | No | No | 39.6 | **0.012** | **0.017** | **0.013** |
| SF3D | **3.5 sec** | Cube projection | **Yes** | No | **48.2** | 0.112 | 0.117 | 0.122 |
| Ours | 10 sec | **Generative** | **Yes** | **Yes** | 35.2 | 0.038 | 0.042 | 0.035 |

the 3-second generation time required by our base model to create a single image. All evaluations were performed on a single A100 GPU.

We used T$^3$Bench (He et al., 2023) for automatic evaluation, measuring both generation quality and prompt alignment of the resulting meshes. T$^3$Bench includes three prompt sets: Single Object, Single Object with Surroundings, and Multiple Objects. Since our model is specifically designed for single-object generation, we focused our evaluation on that track. We used the code provided in the T$^3$Bench repository[2] for comparisons. Overall, we evaluated 100 prompts (see appendix D). Visual comparisons are provided in fig. 9.

T$^3$Bench evaluates only multi-view renderings, it does not assess the underlying mesh quality. To address this, we followed Shen et al. (2023) and calculated metrics such as the percentage of triangle aspect ratios > 4 (**AR>4(%)**), radius ratios > 4 (**RR>4(%)**), and minimum angles < 10 (**MA<10(%)**), using PyVista (Sullivan & Kaszynski, 2019) for all feed-forward methods. While these intrinsic metrics cannot guarantee overall quality, they provide reasonable proxy for some applications.

As shown in table 1, our method achieves competitive results compared to state-of-the-art models, while providing superior editability via separable parts and producing nearly artistic UV maps. Unlike other approaches that rely on vertex colors or pre-defined fixed unwrapping, our method natively generates UV-space textures. This results in more logical chart separation, better area utilization, and sharper details compared to other methods, as demonstrated in fig. 10.

## 4.4 Ablation Study

In this section, we validate our method by ablating key design choices and evaluating their impact. Specifically, we ablated three aspects of our approach: the absence of cross-attention layers in the geometry image branch, the use of the Collaborative Control mechanism, and the cylindrical coordinate transform. To ensure consistency, all experiments used the same batch size, number of steps, and hardware.

First, we reintroduced **cross-attention layers** in the geometry image branch, making it a full architectural clone of the frozen branch. As shown in the second row of fig. 11, while the model still follows the prompts, its generalization ability significantly deteriorates, especially with out-of-distribution prompts like “a steampunk gun”, which is consistent with the observations in Vainer et al. (2024).

Next, we removed the **Collaborative Control** mechanism and fine-tuned the base model to generate both albedo textures and geometry images, concatenating their latents. This resulted in a significant drop in both shape and texture quality, as seen in the third row of fig. 11.

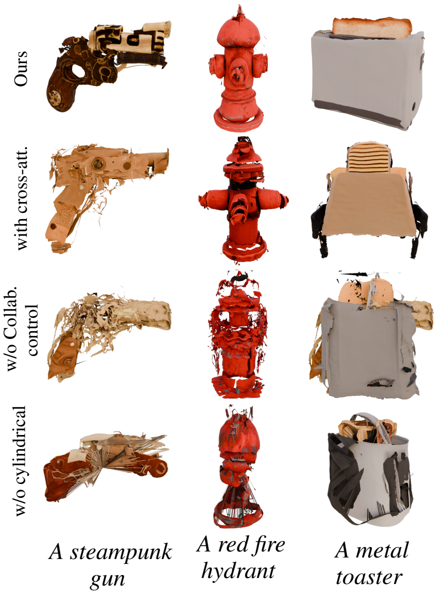

Figure 11: The first row shows our full method’s performance, with subsequent rows removing key design elements.

Finally, we ablated **cylindrical coordinates** by fine-tuning the model as before but omitting the coordinate transformation. Without this step, the model struggled to generate even basic shapes.

[2] https://github.com/THU-LYJ-Lab/T3Bench

### 4.5 Limitations

Our current method has certain limitations. The most common issue is the appearance of visible cracks in the generated meshes. These artifacts result from two key factors: Multi-Chart Geometry Images lack inter-chart connectivity information, and irregular chart boundaries are prone to undersampling (see fig. 12), as analyzed by Sander et al. (2003). The original paper proposed a zippering algorithm to close the cracks between adjacent charts, but this approach assumes the watertightness of the underlying mesh, which is not generally true for real-world meshes. In future work, we aim to generalize and adapt the zippering algorithm. Sampling-related modifications, such as those proposed by Gauthier & Poulin (2009); Yan et al. (2024), could further improve the results.

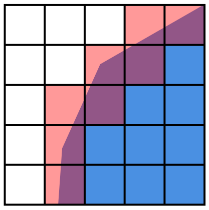

Figure 12: The blue area represents a chart, undersampling at insufficient resolutions can affect chart boundaries. Affected pixels are highlighted in red.

Additionally, we believe this issue is exacerbated by the VAE's latent compression. Areas smaller than $8 \times 8$ pixels fall below the VAE's latent resolution, leading to visual artifacts such as noisy edges and misaligned charts. We hypothesize that integrating wavelets into the VAE, as suggested by Sadat et al. (2024), could mitigate these issues.

Another limitation stems from the discrepancy between the natural image prior and the domain of our model. Although individual charts in a geometry image can be arbitrarily rotated and still represent the same 3D object, the frozen base model is not rotationally equivariant (Weiler et al., 2021). Human faces serve as a good example — while typically upright in natural images, they can appear in random orientations on texture maps, leading to varying quality for such prompts (see examples in appendix B). In future work, we plan to investigate ways to establish canonical orientations for these charts, ensuring better alignment with the diffusion prior.

Additionally, we sometimes observe that the model duplicates parts of the object, which can result in visual artifacts in the generated meshes due to z-fighting. However, the segmented nature of the generated objects makes these artifacts easy to resolve manually.

## 5 Discussion and future work

In this work, we present **Geometry Image Diffusion** (GIMDiffusion), a novel Text-to-3D generation paradigm that utilizes geometry images as its core 3D representation in combination with powerful natural image priors in the form of pre-trained diffusion models. Our results show that GIMDiffusion can generate relightable 3D assets with high-quality UV maps as efficiently as existing Text-to-Image methods generate normal images, while avoiding the need for complex, custom 3D-aware architectures. We believe that our research lays the groundwork for a new direction in Text-to-3D generation.

Future improvements include eliminating visible cracks, achieving better alignment with 2D priors, and enhancing the precision of generations. Incorporating topology prediction and conditioning on specific polygon budgets could provide greater control over the generated 3D objects, making them more practical for gaming and other graphics pipelines. Furthermore, the inherent capability of GIMDiffusion to model both geometry and parameterization makes it particularly well-suited to addressing the longstanding challenge of UV mapping creation for existing geometries. Equally promising is the potential of GIMDiffusion in related fields such as interactive editing, animation and Text-to-Video generation.

### Acknowledgments

Acknowledgments withheld during double-blind review phase.

## References

Josh Achiam, Steven Adler, Sandhini Agarwal, Lama Ahmad, Ilge Akkaya, Florencia Leoni Aleman, Diogo Almeida, Janko Altenschmidt, Sam Altman, Shyamal Anadkat, et al. Gpt-4 technical report. *arXiv preprint arXiv:2303.08774*, 2023.

Hassan Abu Alhaija, Alara Dirik, Andr'e Knorig, Sanja Fidler, and Maria Shugrina. Xdgan: Multi-modal 3d shape generation in 2d space. In *British Machine Vision Conference*, 2022. URL https://api.semanticscholar.org/CorpusID:252734885.

Thiemo Alldieck, Nikos Kolotouros, and Cristian Sminchisescu. Score distillation sampling with learned manifold corrective. *ArXiv*, abs/2401.05293, 2024. URL https://api.semanticscholar.org/CorpusID:266902901.

Raphael Bensadoun, Tom Monnier, Yanir Kleiman, Filippos Kokkinos, Yawar Siddiqui, Mahendra Kariya, Omri Harosh, Roman Shapovalov, Benjamin Graham, Emilien Garreau, Animesh Karnewar, Ang Cao, Idan Azuri, Iurii Makarov, Eric-Tuan Le, Antoine Toisoul, David Novotny, Oran Gafni, Natalia Neverova, and Andrea Vedaldi. Meta 3d gen, 2024. URL https://arxiv.org/abs/2407.02599.

Mark Boss, Zixuan Huang, Aaryaman Vasishta, and Varun Jampani. Sf3d: Stable fast 3d mesh reconstruction with uv-unwrapping and illumination disentanglement. 2024. URL https://api.semanticscholar.org/CorpusID:271600515.

Eric Chan, Connor Z. Lin, Matthew Chan, Koki Nagano, Boxiao Pan, Shalini De Mello, Orazio Gallo, Leonidas J. Guibas, Jonathan Tremblay, S. Khamis, Tero Karras, and Gordon Wetzstein. Efficient geometry-aware 3d generative adversarial networks. *2022 IEEE/CVF Conference on Computer Vision and Pattern Recognition (CVPR)*, pp. 16102–16112, 2021. URL https://api.semanticscholar.org/CorpusID:245144673.

Zhiqin Chen and Hao Zhang. Learning implicit fields for generative shape modeling. *2019 IEEE/CVF Conference on Computer Vision and Pattern Recognition (CVPR)*, pp. 5932–5941, 2018. URL https://api.semanticscholar.org/CorpusID:54457478.

Jasmine Collins, Shubham Goel, Achleshwar Luthra, Leon L. Xu, Kenan Deng, Xi Zhang, T. F. Y. Vicente, Himanshu Arora, T. L. Dideriksen, Matthieu Guillaumin, and Jitendra Malik. Abo: Dataset and benchmarks for real-world 3d object understanding. *2022 IEEE/CVF Conference on Computer Vision and Pattern Recognition (CVPR)*, pp. 21094–21104, 2021. URL https://api.semanticscholar.org/CorpusID:238634701.

Matt Deitke, Dustin Schwenk, Jordi Salvador, Luca Weihs, Oscar Michel, Eli VanderBilt, Ludwig Schmidt, Kiana Ehsani, Aniruddha Kembhavi, and Ali Farhadi. Objaverse: A universe of annotated 3d objects. *2023 IEEE/CVF Conference on Computer Vision and Pattern Recognition (CVPR)*, pp. 13142–13153, 2022. URL https://api.semanticscholar.org/CorpusID:254685588.

Akio Doi and Akio Koide. An efficient method of triangulating equi-valued surfaces by using tetrahedral cells. *IEICE Transactions on Information and Systems*, 74:214–224, 1991. URL https://api.semanticscholar.org/CorpusID:60496605.

Matthijs Douze, Alexandr Guzhva, Chengqi Deng, Jeff Johnson, Gergely Szilvasy, Pierre-Emmanuel Mazaré, Maria Lomeli, Lucas Hosseini, and Hervé Jégou. The faiss library. 2024.

Yiqun Duan, Xianda Guo, and Zhengbiao Zhu. Diffusiondepth: Diffusion denoising approach for monocular depth estimation. *ArXiv*, abs/2303.05021, 2023. URL https://api.semanticscholar.org/CorpusID:257427203.

Patrick Esser, Sumith Kulal, A. Blattmann, Rahim Entezari, Jonas Muller, Harry Saini, Yam Levi, Dominik Lorenz, Axel Sauer, Frederic Boesel, Dustin Podell, Tim Dockhorn, Zion English, Kyle Lacey, Alex Goodwin, Yannik Marek, and Robin Rombach. Scaling rectified flow transformers for high-resolution image synthesis. *ArXiv*, abs/2403.03206, 2024. URL https://api.semanticscholar.org/CorpusID:268247980.

Michael S Floater and Kai Hormann. Surface parameterization: a tutorial and survey. *Advances in multiresolution for geometric modelling*, pp. 157–186, 2005.

Mathieu Gauthier and Pierre Poulin. Preserving sharp edges in geometry images. In *Graphics Interface*, 2009. URL https://api.semanticscholar.org/CorpusID:8077070.

Xianfeng Gu, Steven J. Gortler, and Hugues Hoppe. Geometry images. *Proceedings of the 29th annual conference on Computer graphics and interactive techniques*, 2002. URL https://api.semanticscholar.org/CorpusID:207567120.

Yuze He, Yushi Bai, Matthieu Lin, Wang Zhao, Yubin Hu, Jenny Sheng, Ran Yi, Juanzi Li, and Yong-Jin Liu. T$^3$bench: Benchmarking current progress in text-to-3d generation. *arXiv preprint arXiv:2310.02977*, 2023.

Lukas Höllein, Aljavz Bovzivc, Norman Muller, David Novotny, Hung-Yu Tseng, Christian Richardt, Michael Zollhofer, and Matthias Nießner. Viewdiff: 3d-consistent image generation with text-to-image models. *ArXiv*, abs/2403.01807, 2024. URL https://api.semanticscholar.org/CorpusID:268098692.

Fangzhou Hong, Jiaxiang Tang, Ziang Cao, Min Shi, Tong Wu, Zhaoxi Chen, Tengfei Wang, Liang Pan, Dahua Lin, and Ziwei Liu. 3dtopia: Large text-to-3d generation model with hybrid diffusion priors. *ArXiv*, abs/2403.02234, 2024. URL https://api.semanticscholar.org/CorpusID:268247806.

Yicong Hong, Kai Zhang, Jiuxiang Gu, Sai Bi, Yang Zhou, Difan Liu, Feng Liu, Kalyan Sunkavalli, Trung Bui, and Hao Tan. Lrm: Large reconstruction model for single image to 3d. *ArXiv*, abs/2311.04400, 2023. URL https://api.semanticscholar.org/CorpusID:265050698.

Liucheng Hu, Xin Gao, Peng Zhang, Ke Sun, Bang Zhang, and Liefeng Bo. Animate anyone: Consistent and controllable image-to-video synthesis for character animation. *ArXiv*, abs/2311.17117, 2023. URL https://api.semanticscholar.org/CorpusID:265499043.

Zixuan Huang, Justin Johnson, Shoubhik Debnath, James M. Rehg, and Chao-Yuan Wu. Pointinfinity: Resolution-invariant point diffusion models. 2024. URL https://api.semanticscholar.org/CorpusID:268889290.

Heewoo Jun and Alex Nichol. Shap-e: Generating conditional 3d implicit functions. *ArXiv*, abs/2305.02463, 2023. URL https://api.semanticscholar.org/CorpusID:258480331.

Yash Kant, Ziyi Wu, Michael Vasilkovsky, Guocheng Qian, Jian Ren, Riza Alp Guler, Bernard Ghanem, S. Tulyakov, Igor Gilitschenski, and Aliaksandr Siarohin. Spad : Spatially aware multiview diffusers. *ArXiv*, abs/2402.05235, 2024. URL https://api.semanticscholar.org/CorpusID:267547881.

Tero Karras, Samuli Laine, and Timo Aila. A style-based generator architecture for generative adversarial networks. *2019 IEEE/CVF Conference on Computer Vision and Pattern Recognition (CVPR)*, pp. 4396–4405, 2018. URL https://api.semanticscholar.org/CorpusID:54482423.

Oren Katzir, Or Patashnik, Daniel Cohen-Or, and Dani Lischinski. Noise-free score distillation. *ArXiv*, abs/2310.17590, 2023. URL https://api.semanticscholar.org/CorpusID:264490431.

Bing Wen Ke, Anton Obukhov, Shengyu Huang, Nando Metzger, Rodrigo Caye Daudt, and Konrad Schindler. Repurposing diffusion-based image generators for monocular depth estimation. *ArXiv*, abs/2312.02145, 2023. URL https://api.semanticscholar.org/CorpusID:265609019.

Bernhard Kerbl, Georgios Kopanas, Thomas Leimkuehler, and George Drettakis. 3d gaussian splatting for real-time radiance field rendering. *ACM Transactions on Graphics (TOG)*, 42:1 – 14, 2023. URL https://api.semanticscholar.org/CorpusID:259267917.

Yixun Liang, Xin Yang, Jiantao Lin, Haodong Li, Xiaogang Xu, and Yingcong Chen. Luciddreamer: Towards high-fidelity text-to-3d generation via interval score matching. *ArXiv*, abs/2311.11284, 2023. URL https://api.semanticscholar.org/CorpusID:265295106.

Shanchuan Lin, Bingchen Liu, Jiashi Li, and Xiao Yang. Common diffusion noise schedules and sample steps are flawed. In *Proceedings of the IEEE/CVF Winter Conference on Applications of Computer Vision*, pp. 5404–5411, 2024.

Yaron Lipman, Ricky T Q Chen, Heli Ben-Hamu, Maximilian Nickel, and Matt Le. Flow matching for generative modeling. October 2022.

Ruoshi Liu, Rundi Wu, Basile Van Hoorick, Pavel Tokmakov, Sergey Zakharov, and Carl Vondrick. Zero-1-to-3: Zero-shot one image to 3d object. *2023 IEEE/CVF International Conference on Computer Vision (ICCV)*, pp. 9264–9275, 2023. URL https://api.semanticscholar.org/CorpusID:257631738.

William E. Lorensen and Harvey E. Cline. Marching cubes: A high resolution 3d surface construction algorithm. *Proceedings of the 14th annual conference on Computer graphics and interactive techniques*, 1987. URL https://api.semanticscholar.org/CorpusID:15545924.

Jonathan Lorraine, Kevin Xie, Xiaohui Zeng, Chen-Hsuan Lin, Towaki Takikawa, Nicholas Sharp, Tsung-Yi Lin, Ming-Yu Liu, Sanja Fidler, and James Lucas. Att3d: Amortized text-to-3d object synthesis. *2023 IEEE/CVF International Conference on Computer Vision (ICCV)*, pp. 17900–17910, 2023. URL https://api.semanticscholar.org/CorpusID:259145353.

Tiange Luo, Chris Rockwell, Honglak Lee, and Justin Johnson. Scalable 3d captioning with pretrained models. *arXiv preprint arXiv:2306.07279*, 2023.

Ravi Malladi, James A. Sethian, and Baba C. Vemuri. Shape modeling with front propagation: A level set approach. *IEEE Trans. Pattern Anal. Mach. Intell.*, 17:158–175, 1995. URL https://api.semanticscholar.org/CorpusID:9505101.

Lars M. Mescheder, Michael Oechsle, Michael Niemeyer, Sebastian Nowozin, and Andreas Geiger. Occupancy networks: Learning 3d reconstruction in function space. *2019 IEEE/CVF Conference on Computer Vision and Pattern Recognition (CVPR)*, pp. 4455–4465, 2018. URL https://api.semanticscholar.org/CorpusID:54465161.

Ben Mildenhall, Pratul P. Srinivasan, Matthew Tancik, Jonathan T. Barron, Ravi Ramamoorthi, and Ren Ng. Nerf. *Communications of the ACM*, 65:99 – 106, 2020. URL https://api.semanticscholar.org/CorpusID:213175590.

Alex Nichol, Heewoo Jun, Prafulla Dhariwal, Pamela Mishkin, and Mark Chen. Point-e: A system for generating 3d point clouds from complex prompts. *ArXiv*, abs/2212.08751, 2022. URL https://api.semanticscholar.org/CorpusID:254854214.

Pablo Pernias, Dominic Rampas, Mats L. Richter, Christopher Pal, and Marc Aubreville. Würstchen: An efficient architecture for large-scale text-to-image diffusion models. In *International Conference on Learning Representations*, 2024. URL https://api.semanticscholar.org/CorpusID:271532752.

Dustin Podell, Zion English, Kyle Lacey, A. Blattmann, Tim Dockhorn, Jonas Muller, Joe Penna, and Robin Rombach. Sdxl: Improving latent diffusion models for high-resolution image synthesis. *ArXiv*, abs/2307.01952, 2023. URL https://api.semanticscholar.org/CorpusID:259341735.

Ben Poole, Ajay Jain, Jonathan T. Barron, and Ben Mildenhall. Dreamfusion: Text-to-3d using 2d diffusion. *ArXiv*, abs/2209.14988, 2022. URL https://api.semanticscholar.org/CorpusID:252596091.

Alec Radford, Jong Wook Kim, Chris Hallacy, Aditya Ramesh, Gabriel Goh, Sandhini Agarwal, Girish Sastry, Amanda Askell, Pamela Mishkin, Jack Clark, et al. Learning transferable visual models from natural language supervision. In *International conference on machine learning*, pp. 8748–8763. PMLR, 2021.

Robin Rombach, A. Blattmann, Dominik Lorenz, Patrick Esser, and Björn Ommer. High-resolution image synthesis with latent diffusion models. *2022 IEEE/CVF Conference on Computer Vision and Pattern Recognition (CVPR)*, pp. 10674–10685, 2021. URL https://api.semanticscholar.org/CorpusID:245335280.

Ciara Rowles, Shimon Vainer, Dante De Nigris, Slava Elizarov, Konstantin Kutsy, and Simon Donné. Ipadapter-instruct: Resolving ambiguity in image-based conditioning using instruct prompts, 2024. URL `https://arxiv.org/abs/2408.03209`.

Seyedmorteza Sadat, Jakob Buhmann, Derek Bradley, Otmar Hilliges, and Romann M Weber. Litevae: Lightweight and efficient variational autoencoders for latent diffusion models. *arXiv preprint arXiv:2405.14477*, 2024.

Pedro V. Sander, Zoë J. Wood, Steven J. Gortler, John M. Snyder, and Hugues Hoppe. Multi-chart geometry images. In *Eurographics Symposium on Geometry Processing*, 2003. URL `https://api.semanticscholar.org/CorpusID:4893489`.

Rohan Sawhney and Keenan Crane. Boundary first flattening. *ACM Transactions on Graphics (TOG)*, 37:1 – 14, 2017. URL `https://api.semanticscholar.org/CorpusID:55530`.

Christoph Schuhmann, Romain Beaumont, Richard Vencu, Cade Gordon, Ross Wightman, Mehdi Cherti, Theo Coombes, Aarush Katta, Clayton Mullis, Mitchell Wortsman, Patrick Schramowski, Srivatsa Kundurthy, Katherine Crowson, Ludwig Schmidt, Robert Kaczmarczyk, and Jenia Jitsev. Laion-5b: An open large-scale dataset for training next generation image-text models. *ArXiv*, abs/2210.08402, 2022. URL `https://api.semanticscholar.org/CorpusID:252917726`.

Tianchang Shen, Jacob Munkberg, Jon Hasselgren, Kangxue Yin, Zian Wang, Wenzheng Chen, Zan Gojcic, Sanja Fidler, Nicholas Sharp, and Jun Gao. Flexible isosurface extraction for gradient-based mesh optimization. *ACM Trans. Graph.*, 42(4):37–1, 2023.

Ruoxi Shi, Hansheng Chen, Zhuoyang Zhang, Minghua Liu, Chao Xu, Xinyue Wei, Linghao Chen, Chong Zeng, and Hao Su. Zero123++: a single image to consistent multi-view diffusion base model. *ArXiv*, abs/2310.15110, 2023a. URL `https://api.semanticscholar.org/CorpusID:264436559`.

Yichun Shi, Peng Wang, Jianglong Ye, Mai Long, Kejie Li, and X. Yang. Mvdream: Multi-view diffusion for 3d generation. *ArXiv*, abs/2308.16512, 2023b. URL `https://api.semanticscholar.org/CorpusID:261395233`.

Yawar Siddiqui, Tom Monnier, Filippos Kokkinos, Mahendra Kariya, Yanir Kleiman, Emilien Garreau, Oran Gafni, Natalia V. Neverova, Andrea Vedaldi, Roman Shapovalov, and David Novotny. Meta 3d assetgen: Text-to-mesh generation with high-quality geometry, texture, and pbr materials. *ArXiv*, abs/2407.02445, 2024. URL `https://api.semanticscholar.org/CorpusID:270878069`.

Ayan Sinha, Jing Bai, and Karthik Ramani. Deep learning 3d shape surfaces using geometry images. In *European Conference on Computer Vision*, 2016. URL `https://api.semanticscholar.org/CorpusID:8846709`.

Jascha Sohl-Dickstein, Eric A Weiss, Niru Maheswaranathan, and Surya Ganguli. Deep unsupervised learning using nonequilibrium thermodynamics. March 2015.

Yang Song, Jascha Narain Sohl-Dickstein, Diederik P. Kingma, Abhishek Kumar, Stefano Ermon, and Ben Poole. Score-based generative modeling through stochastic differential equations. *ArXiv*, abs/2011.13456, 2020. URL `https://api.semanticscholar.org/CorpusID:227209335`.

Pratul P. Srinivasan, Stephan J. Garbin, Dor Verbin, Jonathan T. Barron, and Ben Mildenhall. Nuvo: Neural uv mapping for unruly 3d representations. *ArXiv*, abs/2312.05283, 2023. URL `https://api.semanticscholar.org/CorpusID:266162619`.

C. Bane Sullivan and Alexander Kaszynski. PyVista: 3d plotting and mesh analysis through a streamlined interface for the visualization toolkit (VTK). *Journal of Open Source Software*, 4(37): 1450, may 2019. doi: 10.21105/joss.01450. URL `https://doi.org/10.21105/joss.01450`.

Jiaxiang Tang, Jiawei Ren, Hang Zhou, Ziwei Liu, and Gang Zeng. Dreamgaussian: Generative gaussian splatting for efficient 3d content creation. *arXiv preprint arXiv:2309.16653*, 2023.

Jiaxiang Tang, Zhaoxi Chen, Xiaokang Chen, Tengfei Wang, Gang Zeng, and Ziwei Liu. Lgm: Large multi-view gaussian model for high-resolution 3d content creation. *ArXiv*, abs/2402.05054, 2024. URL `https://api.semanticscholar.org/CorpusID:267523413`.

Dmitry Tochilkin, David Pankratz, Zexiang Liu, Zixuan Huang, Adam Letts, Yangguang Li, Ding Liang, Christian Laforte, Varun Jampani, and Yan-Pei Cao. Triposr: Fast 3d object reconstruction from a single image. *ArXiv*, abs/2403.02151, 2024. URL `https://api.semanticscholar.org/CorpusID:268248244`.

Shimon Vainer, Mark Boss, Mathias Parger, Konstantin Kutsy, Dante De Nigris, Ciara Rowles, Nicolas Perony, and Simon Donn'e. Collaborative control for geometry-conditioned pbr image generation. *ArXiv*, abs/2402.05919, 2024. URL `https://api.semanticscholar.org/CorpusID:267547446`.

Ashish Vaswani, Noam M. Shazeer, Niki Parmar, Jakob Uszkoreit, Llion Jones, Aidan N. Gomez, Lukasz Kaiser, and Illia Polosukhin. Attention is all you need. In *Neural Information Processing Systems*, 2017. URL `https://api.semanticscholar.org/CorpusID:13756489`.

Haochen Wang, Xiaodan Du, Jiahao Li, Raymond A. Yeh, and Gregory Shakhnarovich. Score jacobian chaining: Lifting pretrained 2d diffusion models for 3d generation. *2023 IEEE/CVF Conference on Computer Vision and Pattern Recognition (CVPR)*, pp. 12619–12629, 2022. URL `https://api.semanticscholar.org/CorpusID:254125253`.

Zhengyi Wang, Cheng Lu, Yikai Wang, Fan Bao, Chongxuan LI, Hang Su, and Jun Zhu. Prolificdreamer: High-fidelity and diverse text-to-3d generation with variational score distillation. In A. Oh, T. Naumann, A. Globerson, K. Saenko, M. Hardt, and S. Levine (eds.), *Advances in Neural Information Processing Systems*, volume 36, pp. 8406–8441. Curran Associates, Inc., 2023. URL `https://proceedings.neurips.cc/paper_files/paper/2023/file/1a87980b9853e84dfb295855b425c262-Paper-Conference.pdf`.

Zhengyi Wang, Yikai Wang, Yifei Chen, Chendong Xiang, Shuo Chen, Dajiang Yu, Chongxuan Li, Hang Su, and Jun Zhu. Crm: Single image to 3d textured mesh with convolutional reconstruction model. *arXiv preprint arXiv:2403.05034*, 2024.

Maurice Weiler, Patrick Forr'e, Erik P. Verlinde, and Max Welling. Coordinate independent convolutional networks - isometry and gauge equivariant convolutions on riemannian manifolds. *ArXiv*, abs/2106.06020, 2021. URL `https://api.semanticscholar.org/CorpusID:235417099`.

Zike Wu, Pan Zhou, Xuanyu Yi, Xiaoding Yuan, and Hanwang Zhang. Consistent3d: Towards consistent high-fidelity text-to-3d generation with deterministic sampling prior. *ArXiv*, abs/2401.09050, 2024. URL `https://api.semanticscholar.org/CorpusID:267027883`.

Kevin Xie, Jonathan Lorraine, Tianshi Cao, Jun Gao, James Lucas, Antonio Torralba, Sanja Fidler, and Xiaohui Zeng. Latte3d: Large-scale amortized text-to-enhanced3d synthesis. *ArXiv*, abs/2403.15385, 2024. URL `https://api.semanticscholar.org/CorpusID:268667414`.

Yiheng Xie, Towaki Takikawa, Shunsuke Saito, Or Litany, Shiqin Yan, Numair Khan, Federico Tombari, James Tompkin, Vincent Sitzmann, and Srinath Sridhar. Neural fields in visual computing and beyond. *Computer Graphics Forum*, 41, 2021. URL `https://api.semanticscholar.org/CorpusID:244478496`.

Jiazheng Xu, Xiao Liu, Yuchen Wu, Yuxuan Tong, Qinkai Li, Ming Ding, Jie Tang, and Yuxiao Dong. Imagereward: Learning and evaluating human preferences for text-to-image generation. *Advances in Neural Information Processing Systems*, 36, 2024.

Xingguang Yan, Han-Hung Lee, Ziyu Wan, and Angel X. Chang. An object is worth 64x64 pixels: Generating 3d object via image diffusion. 2024. URL `https://api.semanticscholar.org/CorpusID:271719920`.

Lior Yariv, Omri Puny, Natalia V. Neverova, Oran Gafni, and Yaron Lipman. Mosaic-sdf for 3d generative models. *ArXiv*, abs/2312.09222, 2023. URL `https://api.semanticscholar.org/CorpusID:266209832`.

Hu Ye, Jun Zhang, Sibo Liu, Xiao Han, and Wei Yang. Ip-adapter: Text compatible image prompt adapter for text-to-image diffusion models. *arXiv preprint arXiv:2308.06721*, 2023.

Taoran Yi, Jiemin Fang, Guanjun Wu, Lingxi Xie, Xiaopeng Zhang, Wenyu Liu, Qi Tian, and Xinggang Wang. Gaussiandreamer: Fast generation from text to 3d gaussian splatting with point cloud priors. *arXiv preprint arXiv:2310.08529*, 2023.

Jonathan Young. Xatlas: Mesh parameterization / uv unwrapping library. `https://github.com/jpcy/xatlas`, 2022.

Denis Zavadski, Johann-Friedrich Feiden, and Carsten Rother. Controlnet-xs: Designing an efficient and effective architecture for controlling text-to-image diffusion models. *ArXiv*, abs/2312.06573, 2023. URL `https://api.semanticscholar.org/CorpusID:266162697`.

Xiaohui Zeng, Arash Vahdat, Francis Williams, Zan Gojcic, Or Litany, Sanja Fidler, and Karsten Kreis. Lion: Latent point diffusion models for 3d shape generation. *ArXiv*, abs/2210.06978, 2022. URL `https://api.semanticscholar.org/CorpusID:252872881`.

Lvmin Zhang, Anyi Rao, and Maneesh Agrawala. Adding conditional control to text-to-image diffusion models. *2023 IEEE/CVF International Conference on Computer Vision (ICCV)*, pp. 3813–3824, 2023. URL `https://api.semanticscholar.org/CorpusID:256827727`.

Richard Zhang, Phillip Isola, Alexei A Efros, Eli Shechtman, and Oliver Wang. The unreasonable effectiveness of deep features as a perceptual metric. In *CVPR*, 2018.

Chuanxia Zheng and Andrea Vedaldi. Free3d: Consistent novel view synthesis without 3d representation. *ArXiv*, abs/2312.04551, 2023. URL `https://api.semanticscholar.org/CorpusID:266052796`.

Xin Zheng, Yang Liu, Peng-Shuai Wang, and Xin Tong. Sdf-stylegan: Implicit sdf-based stylegan for 3d shape generation. *Computer Graphics Forum*, 41, 2022. URL `https://api.semanticscholar.org/CorpusID:250048592`.

Junzhe Zhu, Peiye Zhuang, and Oluwasanmi Koyejo. Hifa: High-fidelity text-to-3d generation with advanced diffusion guidance. In *International Conference on Learning Representations*, 2023. URL `https://api.semanticscholar.org/CorpusID:258967476`.

# A VAE DESIGN AND TRAINING DETAILS

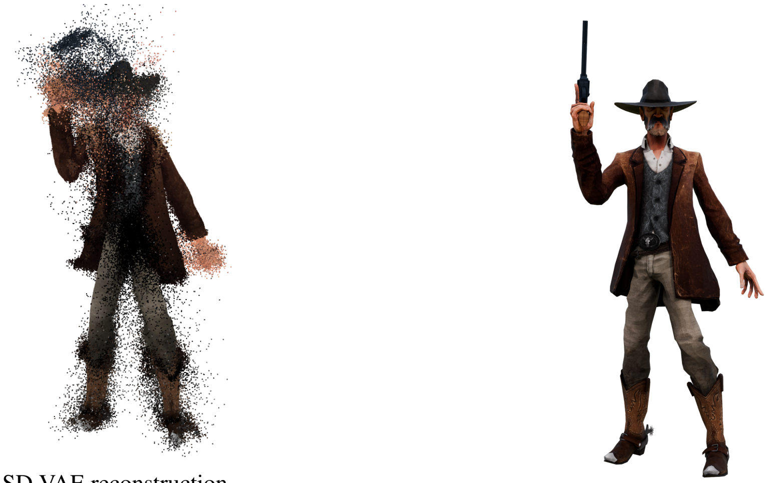

SD VAE reconstruction

GIM VAE reconstruction

Figure 13: Comparison of geometry reconstruction between the SD VAE and our GIM VAE. The SD VAE reconstruction could not be meaningfully triangulated, a point cloud is visualized instead of a mesh

The Stable Diffusion Variational Autoencoder (SD VAE) is trained on natural images and achieves high reconstruction quality in that domain. However, it does not transfer well to the domain of geometry images.

The first issue is that the reconstructed images contain a considerable amount of noise (see fig. 13). While these perturbations may be imperceptible in the image domain, they cause significant problems in the 3D domain, such as the loss of fine geometric details. We hypothesize that this behavior arises from the LPIPS (Zhang et al., 2018) and GAN losses used during training, as GANs are known for introducing high-frequency noise into images.

The second issue is the color range bias of the SD VAE, which favors the most common colors in natural images. When applied to points in 3D space, this bias can cause undesirable warping and other artifacts.

Lastly, the original VAE struggles to accurately reconstruct discontinuities at chart boundaries, which is critical for triangulation (see section 3.3.3). Convolutional layers tend to interpolate across boundaries, leading to false geometry due to the creation of smooth transitions instead of sharp ones.

Table 2: VAE evaluations

| Method | Latent dim | PSNR ↑ |
|---|---|---|
| SD VAE | $96 \times 96 \times 4$ | 31.87 |
| GIM VAE | $96 \times 96 \times 8$ | 49.02 |

To address these issues, we made the following design choices:

- **Disentangling chart boundaries from geometry:** We introduced additional input and output channels for a multi-chart mask. This mask can be thresholded to model sharp boundaries, avoiding interpolation artifacts.
- **Removing GAN and perceptual losses:** These were removed to prevent noise from being introduced during training.
- **Increasing latent dimension:** We expanded the latent dimension to 8 to better capture geometric details.

We trained our VAE following the procedure and codebase[3] of Stable Diffusion (Rombach et al., 2021). The model was trained on 8 A100 GPUs with a batch size of 128 for 100k steps. The PSNR results are reported in table 2.

## B Failure cases

Charts in the Geometry Image layout can be randomly rotated without affecting the resulting 3D shape, as this rotation alters only the parameterization. However, GIMDiffusion relies on Stable Diffusion 2.1 as a prior, which is not rotationally equivariant and exhibits strong orientational biases for certain features. For example, it struggles to reliably generate an upside-down face. Consequently, the quality of generated outputs may degrade for certain prompts. With the prompt *"human head"*, for instance, the quality can vary depending on the seed, particularly when the chart containing the face is oriented unfavorably.

Fortunately, GIMDiffusion's fast inference speed enables efficient seed exploration to achieve the desired quality. In future work, we aim to introduce canonical orientations for charts to mitigate this issue.

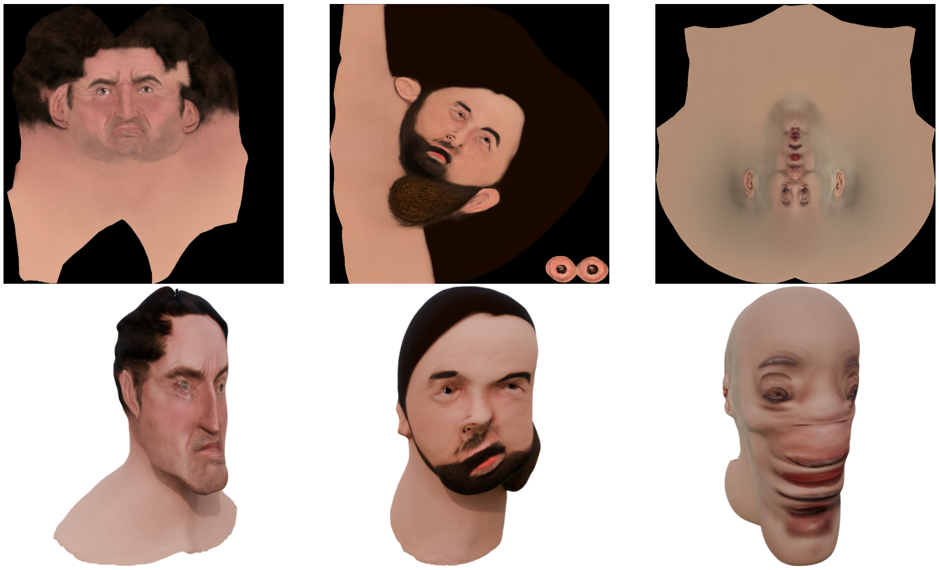

**Prompt:** *A human head*

Figure 14: Generation results for *human head* for three different seeds.

## C Evaluation details

$T^3$Bench (He et al., 2023) evaluates both quality and alignment in text-to-3D generation. Quality is assessed through a standardized multi-view rendering pipeline provided by the authors. This process generates 2D images of the 3D object from various angles and uses scoring models (Radford et al., 2021; Xu et al., 2024) to evaluate overall visual consistency and fidelity. To spot issues such as view inconsistency (e.g., the Janus problem), a regional convolution technique is applied. Alignment measures the semantic consistency between the generated 3D object and the input text prompts using a multi-view captioning process coupled with GPT-4 (Achiam et al., 2023) evaluation. The final score is computed as the average of the quality and alignment metrics.

To compare our method with state-of-the-art image-to-3D approaches, we generated a set of images based on the $T^3$Bench evaluation prompts (see appendix D) using the same base model as our method (Stable Diffusion 2.1). For compatibility with image-to-3D methods, we appended the phrase *"single object, uniform background"* to each prompt. For each prompt, three images were generated, and the

[3] https://github.com/Stability-AI/generative-models

one best aligning with the text and depicting the object from natural angles was manually selected. Figure 15 showcases several examples.

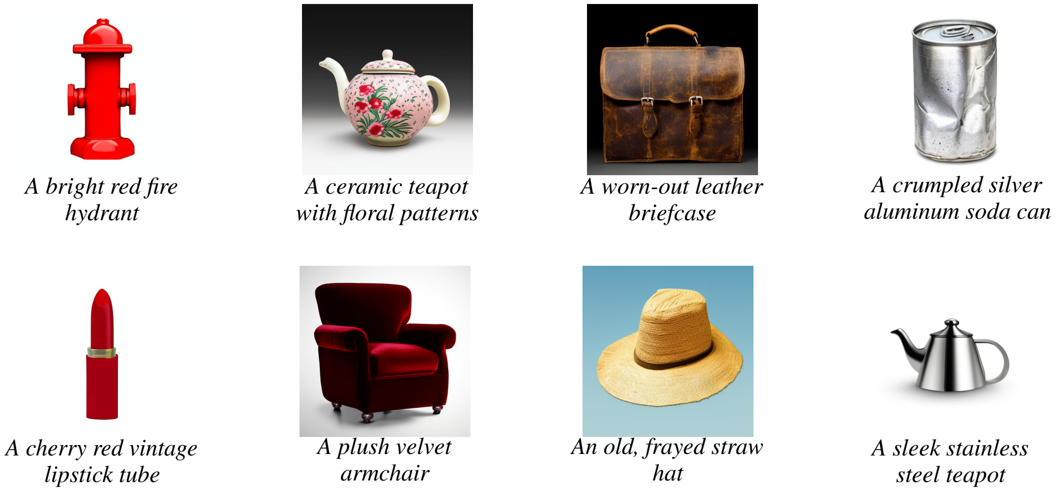

*A bright red fire hydrant*

*A ceramic teapot with floral patterns*

*A worn-out leather briefcase*

*A crumpled silver aluminum soda can*

*A cherry red vintage lipstick tube*

*A plush velvet armchair*

*An old, frayed straw hat*

*A sleek stainless steel teapot*

Figure 15: Examples of images used to condition Image-to-3D models during evaluation.

## D EVALUATION PROMPTS

1. A cactus with pink flowers
2. A rainbow-colored umbrella
3. An antique wooden rocking horse
4. A golden retriever with a blue bowtie
5. An ivory candlestick holder
6. A pair of polka-dotted sneakers
7. A steaming mug of hot chocolate with whipped cream
8. A bright red fire hydrant
9. A gleaming silver saxophone
10. A leather-bound book with gold details
11. A vibrant sunflower with green leaves
12. A castle-shaped sandcastle
13. A neon green skateboard with black wheels
14. A pirate flag with skull and crossbones
15. A plush teddy bear with a satin bow
16. A ripe watermelon sliced in half
17. A sparkling diamond ring in a velvet box
18. A vintage porcelain doll with a frilly dress
19. A chameleon perched on a tree branch
20. A tarnished brass pocket watch
21. A ceramic teapot with floral patterns
22. An antique ruby-studded brooch
23. A simple burgundy colored feather quill
24. A vintage iron-cast typewriter
25. A shiny emerald green beetle
26. A crystal glass paperweight with abstract design
27. A velvet cushion stitched with golden threads
28. A small porcelain white rabbit figurine
29. A left-handed electric guitar painted black
30. A bright blue plastic swimming goggles
31. A partly broken shell of a tortoise
32. A long woolen scarf, striped red and black
33. A tattered old explorer’s map
34. A well-used black iron frying pan
35. A crumpled silver aluminum soda can
36. A thick, green-spined book with yellowed pages
37. A shimmering emerald pendant necklace
38. A well-worn straw sun hat
39. A tarnished silver letter opener
40. An antique glass perfume bottle
41. A polished mahogany grand piano
42. A dented brass trumpet
43. A pristine white wedding gown
44. A chipped porcelain teacup
45. A rustic wrought-iron candle holder
46. A vibrant, handmade patchwork quilt
47. A plush velvet armchair
48. A sleek, black top hat
49. A paint-splattered easel
50. A bent steel crowbar
51. A crisp paper airplane
52. A worn-out rubber tire swing
53. An intricately-carved wooden chess set
54. A bright red kite with a frayed tail
55. A smooth, round opal stone
56. A rusty, vintage metal key
57. A delicate, handmade lace doily
58. A sturdy mahogany walking cane
59. A sparkling crystal chandelier
60. A worn-out red flannel shirt
61. A cracked porcelain doll’s face

62. A dusty classic typewriter
63. A glossy grand black piano
64. A faux-fur leopard print hat
65. A futuristic, sleek electric car model
66. A cherry red vintage lipstick tube
67. A cobweb-covered old wooden chest
68. A gold glittery carnival mask
69. A tattered world map with stained edges
70. A shiny red apple
71. A worn-out leather briefcase
72. An antique gold pocket watch
73. A sleek, slim smartphone
74. A wet, vibrant beach ball
75. A rusty, abandoned bicycle
76. A fluffy, orange cat
77. Crisp, folded origami paper
78. A shiny, new electric guitar
79. A weather-beaten wooden bat
80. A delicate crystal champagne flute
81. An old, frayed straw hat
82. A scuffed up soccer ball
83. A pair of worn-in blue jeans
84. A well-loved stuffed teddy bear
85. A chipped, white coffee mug
86. A bright, yellow rubber duck
87. A sleek stainless steel teapot
88. A water-streaked glass window pane
89. An intricate ceramic vase with peonies painted on it
90. A fuzzy pink flamingo lawn ornament
91. A blooming potted orchid with purple flowers
92. An old bronze ship's wheel
93. A sparkling diamond tiara
94. A vintage plaid woolen blanket
95. A pair of shiny black patent leather shoes
96. An elegant feather-quill ink pen
97. A fragrant pine Christmas wreath
98. A silver mirror with ornate detailing
99. A green enameled watering can
100. A classic leatherette radio with dials

## E LAYOUT NOVELTY

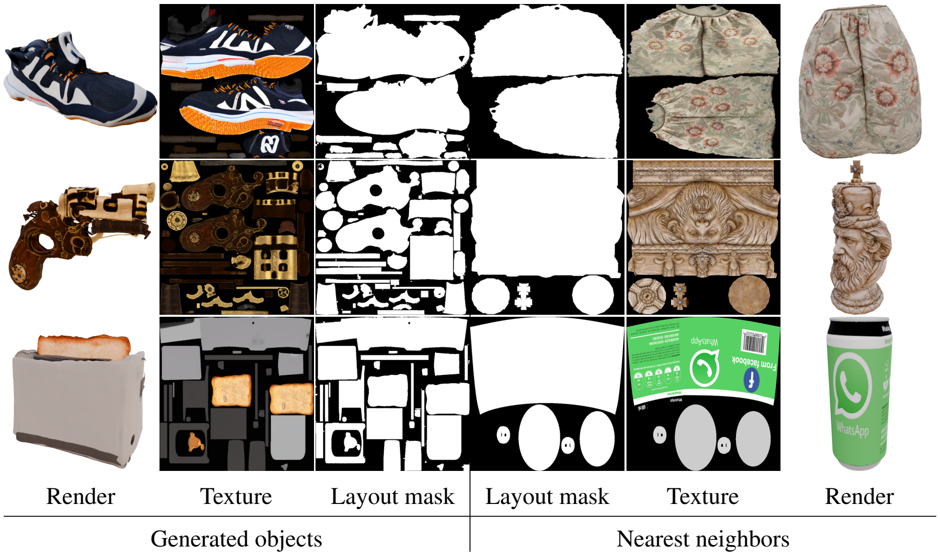

Figure 16: Each row displays a generated object alongside its nearest neighbor by layout mask from the dataset. The nearest UV layouts differ significantly from the corresponding generated ones, often representing entirely different object types.

To demonstrate our model's ability to generate novel UV layouts not present in the training data, we visualize dataset entries that are closest to the generated samples in terms of layout similarity. For this purpose, we constructed an index of binary multi-chart masks extracted from all geometry images in our dataset using the Faiss library Douze et al. (2024). We then queried this index to find the nearest neighbors for the generated samples.

During the training phase of our model, the input data were augmented with random rotations by angles that are multiples of 90 degrees. Accordingly, for each query image, we computed the nearest neighbors across four rotations and selected the neighbor with the lowest Euclidean distance.

The visualizations in fig. 16 reveal that there are non-trivial differences between the generated layouts and those present in the training data, highlighting the model's capability for generating novel layouts.